Shape-Controlled Synthesis of Colloidal Nanorods and Nanoparticles of Barium Titanium Sulfide

Daniel Zilevu, Sidney E. Creutz*

Department of Chemistry, Mississippi State University, Mississippi State, MS 39762, United States

*screutz@chemistry.msstate.edu

ABSTRACT: Ternary transition metal sulfides with the general formula (AE)$M^{IV}S_3$ (AE = Ca, Sr, Ba; M = Zr, Ti, Hf) have recently drawn increasing attention because of their optical, electronic, and thermal properties, with possible applications including photovoltaic absorbers and NIR detectors. However, synthetic routes to these materials, especially as nanomaterials, remain limited. Here, we report the synthesis of $BaTiS_3$ as colloidal nanomaterials using a solution-based, wet-chemical approach at temperatures as low as 280 °C through the use of reactive metal amide precursors. We demonstrate that nanoparticles or nanorods with typical aspect ratios of approximately 8:1 (50 nm length, 6 nm width) can be prepared, with synthetic control over the nanocrystal size and shape afforded through choice of synthetic method (heat-up or hot-injection) and through modulation of the reaction temperature and concentration. Structural data (powder X-ray diffraction) shows the hallmarks of a composite crystal correlated with deviations from the ideal stoichiometry. The $BaTiS_3$ nanorods show a strong and tunable NIR absorbance (~0. 8 eV) whose energy is correlated to the nanorod structure and stoichiometry. These results provide proof of principle for the synthesis of nanocrystals of this class of materials using solution routes.

Ternary alkaline earth metal/Group IV d^0 metal chalcogenides with the general formula (AE)$M^{IV}E_3$ (AE = Ca, Sr, Ba; M = Zr, Ti, Hf; E = S, Se) constitute an emerging class of semiconductor materials with a range of promising optoelectronic properties.[1-3] While members of this class that adopt a perovskite structure (such as $BaZrS_3$) have drawn the most attention as potential photovoltaic materials, recent investigations have shown that other non-perovskite materials such as barium titanium sulfide ($BaTiS_3$) are also characterized by several unusual and potentially useful properties that originate from their composition and structure.

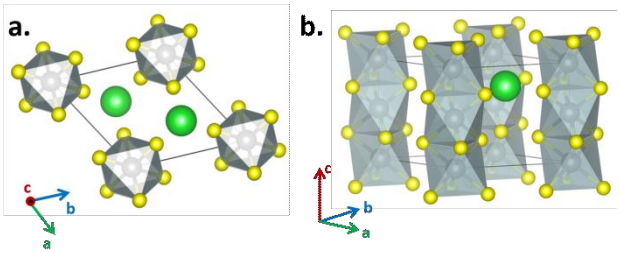

Figure 1. Two views of the unit cell of hexagonal-phase $BaTiS_3$, looking down along the *c*-axis (**a**) and viewed from the side, showing the face-sharing chains of TiS_6 octahedra (**b**). Yellow = S; gray = Ti; green = Ba.

$BaTiS_3$ adopts a hexagonal phase (*P*6_3*mc* or *P*6_3*/mmc*) which is characterized by chains of face-sharing TiS_6 octahedra interspersed with Ba^{2+} cations (Figure 1).[4-6] Due in part to the highly anisotropic nature of the structure—containing one-dimensional chains of TiS_6 units—the material exhibits significant optical anisotropy, including both dichroism and birefringence. Because of the low bandgap of the material (~0.3 eV), the dichroism extends well into the mid-IR, and the birefringence of the material extends throughout the mid-IR and near-IR regions to at least 16 μm, based on the work of Niu *et al.*[7] $BaTiS_3$ shows a birefringence of up to 0.76 in the mid-IR, measured for light polarized perpendicular or parallel to the material's *c*-axis; this value was unprecedented for any homogeneous crystalline solid.[7] This record birefringence is believed to stem in part from the large differences in polarizability between the constituent ions, including the "hard" (low polarizability) Ti^{4+} cation, the relatively softer Ba^{2+} cation, and the soft (highly polarizable) sulfide anion.[8] The material also shows record optical anisotropy (differential absorbance polarized perpendicular or parallel to the *c*-axis) in the visible range.[9]

Beyond its optical properties, the transport properties of $BaTiS_3$ are also unusual. Again, due to the quasi-one dimensional structure, the materials show highly anisotropic thermal and electronic transport properties.[10] $BaTiS_3$ has also been shown to exhibit extremely low and "glass-like" thermal conductivity, which has been attributed to the fact that the Ti^{4+} cations reside in, and can tunnel between, a shallow double potential well. This property is intimately related to the chemistry of this material, and in particular the nature of the bonding interactions between Ti^{4+} and the soft sulfide anions.[11]

Studies of $BaTiS_3$ and related materials have thus far used bulk materials (single crystals or microcrystalline powders). The preparation and study of these materials as colloidal nanocrystals could broaden their potential applications, as well as giving insight to their physical and chemical properties through examination of size- and shape-dependent optical properties and studies of their surface properties.

Chemistry and known synthetic routes. The M^{IV}-S (M^{IV} = Ti, Zr, Hf) bonds in $BaTiS_3$ and other (AE)$M^{IV}E_3$ chalcogenide materials exhibit a higher degree of covalency than the analogous M-O bonds, which means many of these chalcogenide materials have potential as semiconductors with mid-to-

narrow bandgaps and reasonable charge transport properties. At the same time, these materials are chemically unusual (relative to other well-known chalcogenide (E = S, Se) semiconductors such as CdE, PbE, ZnE, $CuInE_2$, etc) in part because of the hard-soft Lewis acid-base mismatch between the highly oxophilic early transition metals (Ti, Zr, Hf) and the sulfide or selenide anion. Despite the oxophilicity of these metals, experimental evidence suggests that chalcogenide perovskites such as $BaZrS_3$ are highly environmentally stable, including in an aqueous environment and up to 550 °C in air,[12-14] in marked contrast to most halide perovskites.

Synthetic routes to $(AE)M^{IV}E_3$ materials can largely be divided into two classes of approaches, both requiring harsh (high-temperature) conditions: (1) high-temperature combination of binary sulfides and/or elemental precursors (furnace at ~450-1000 °C; temperatures at the low end of this range were achieved through the incorporation of halides such as I_2 or $BaCl_2$)[15] or (2) sulfurization of oxide precursors using CS_2 or H_2S at high temperatures (700-1000 °C).[16-18] The latter approach has been successfully used to prepare thin films of $BaZrS_3$ from precursor $BaZrO_3$ films.[19] Thin films of $BaZrS_3$ were also successfully produced by room-temperature sputtering, although thermal treatment to at least 650 °C was required to achieve measurable crystallinity.[20] Additionally, it has recently been demonstrated that large nanocrystals of $BaZrS_3$ produced through solid-phase synthesis could be dispersed in solvent and processed into thin-film transistors.[21] $BaTiS_3$ synthesis is less well explored, and preparations of $BaTiS_3$ as thin films or nanocrystals have not yet been reported.

Solution-phase wet-chemistry approaches to the $(AE)M^{IV}E_3$ materials including $BaTiS_3$ are generally lacking. This may in part be due to the high temperatures apparently necessary to access these materials in crystalline form. However, solution synthesis, particularly of colloidal nanocrystals, would open the door to the development of colloidal inks and thin film precursors. Size and shape control that may be attainable via solution synthesis could lead to greater tunability of the optical, electronic, and thermal properties of the materials, as well as contributing to a greater understanding of structure-function relationships underlying their properties. For these reasons, we have been interested in pursuing synthetic routes to colloidal nanomaterials of $BaTiS_3$ nanomaterials in organic surfactant solution.

Here, we report the preparation of colloidal nanocrystals of $BaTiS_3$ using solution chemistry in oleylamine at readily accessible temperatures. We demonstrate that the shape and size of the nanocrystals can be tuned through variation of the synthetic conditions. A switch in shape between nanorods and nanoparticles under different conditions is correlated with changes in the structure and stoichiometry of the material. Variable optical properties are reported, including strong absorbance in the near-IR. This work brings to light some intriguing and tunable properties of $BaTiS_3$ and serves as proof-of-principle for the preparation of $(AE)M^{IV}E_3$ through wet-chemical routes.

RESULTS AND DISCUSSION

Synthetic approach to colloidal $BaTiS_3$ nanomaterials. The choice of precursors, solvents, and reaction conditions for the successful synthesis of $BaTiS_3$ should fulfill at least two main criteria: (1) the chosen precursors must be sufficiently reactive to readily convert to the desired material at attainable temperatures and (2) the precursors and reaction conditions must be kept rigorously free of water, oxygen, and any oxygen-containing ligands in order to circumvent the thermodynamically favorable formation of undesired $BaTiO_3$ or TiO_2 phases. With these requirements in mind, we targeted the combination of reactive metal organoamide complexes as metal precursors, which are dissolved in oleylamine as a high-boiling amine surfactant (Figure 2).

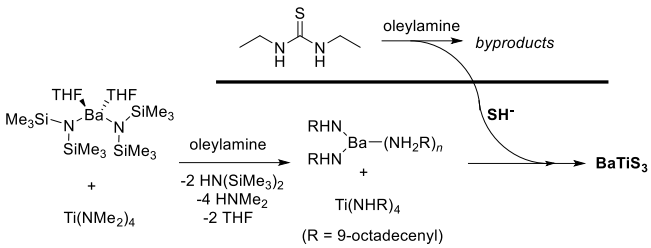

Figure 2. Proposed precursor conversion chemistry involved in the formation of $BaTiS_3$ nanorods.

It is likely that upon dissolution in oleylamine at high temperatures, a protolytic exchange takes place and metal oleylamide complexes result, although we have not characterized the products of this exchange (Figure 2). Several sulfur precursor sources were tested, including elemental sulfur in oleylamine, thioacetamide, carbon disulfide, tetramethylthiourea, and N,N'-diethylthiourea. Of these, the thioureas have most readily produced crystalline, phase-pure $BaTiS_3$ nanocrystals in our hands, and N,N'-diethylthiourea was chosen as the sulfur precursor to be used for further optimization. The use of substituted thioureas as tunable and controllable precursors for sulfide nanocrystal synthesis has been extensively explored; their decomposition in oleylamine solution is hypothesized to formally release H_2S which, upon reaction with the metal precursors, is responsible for nanocrystal formation.[22-24]

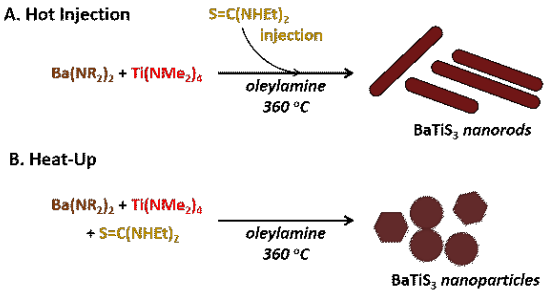

Figure 3. Synthetic approaches used in the formation of nanorods (hot injection, A) and nanoparticles (heat-up, B) of $BaTiS_3$.

Two synthetic approaches to initiate the formation of the $BaTiS_3$ nanocrystals were explored—a *hot-injection* approach where a solution of the sulfur precursor was injected into a solution of metal precursors that had been heated to 360 °C under N_2; and a *heat-up* approach where the precursors were combined in oleylamine at room temperature and heated together to 360 °C (Figure 3). Detailed procedures are provided in the Experimental Methods section. In both cases, a 1:1:30 Ba:Ti:S molar ratio of precursors was used as the standard conditions, and reaction times from <1 minute to 14 hours were tested. The concentration of the reactants was varied by changing the amount of the oleylamine solvent/surfactant used, resulting in metal precursor concentrations ranging from 0.01 – 0.03 M. We found that a high temperature was critical for producing crystalline materials; at temperatures

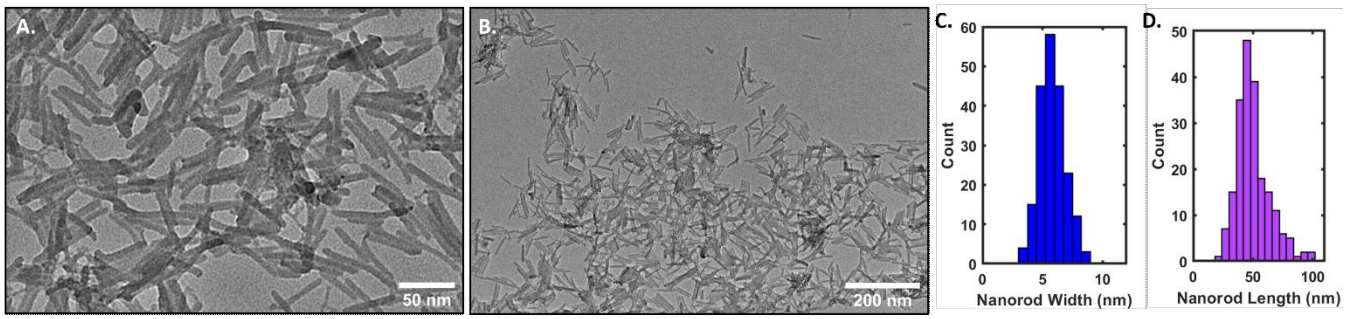

Figure 4. Characterization of a representative $BaTiS_3$ nanorod sample synthesized using a hot-injection approach and standard conditions as described in the text. (A, B) TEM images at different magnification levels; scale bars (white) are 50 nm (A) and 200 nm (B); additional TEM images are provided in the Supporting Information. Histograms of nanorod width (C) and length (D) were tabulated on the basis of measurements of at least 200 individual nanocrystals. The average width is 5.8 ± 1.1 nm and the average length is 47 ± 14 nm.

below 280 °C, we could not observe evidence for the formation of crystalline $BaTiS_3$ by PXRD.

Hot-injection synthesis: $BaTiS_3$ nanorods. The hot-injection synthesis produced $BaTiS_3$ nanorods with aspect ratios ranging from approximately (1.4:1) to (10:1) depending on the reaction conditions. In brief, $Ba[N(SiMe_3)_2]_2(THF)_2$ and $Ti(NMe_2)_4$ are combined in dry oleylamine, heated to 360 °C, and then a solution of N,N'-diethylthiourea preheated to 120 °C in oleylamine is rapidly injected, resulting in an immediate color change to a black suspension. After the desired reaction time was reached, the reaction mixture was cooled to room temperature and the nanocrystals could be isolated and washed with chloroform and ethanol. We found that the resulting nanorods could be readily suspended in chloroform (and other nonpolar solvents such as toluene or tetrachloroethylene) to form well-dispersed colloids, provided sufficient oleylamine is present as a ligand; repeated washing tends to result in a loss of colloidal stability, presumably due to the removal of the relatively weakly bound oleylamine ligands, but solubility can be restored through the addition of ~60 µL of oleylamine to the nanocrystal suspension. Representative TEM data for a nanorod sample synthesized under standard conditions is shown in Figure 4, and a UV-Vis-NIR spectrum of the colloidal solution is shown in Figure 5A.

Powder X-ray diffraction (PXRD) patterns for nanorod samples present a reasonable qualitative match with the predicted PXRD pattern of $BaTiS_3$ in the $BaNiO_3$ structure type ($P6_3/mmc$, Figure 5B);[6, 25] the deviations observed from the expected positions for some features will be discussed below. Scherrer broadening of the diffraction peaks due to the small width of nanorods is apparent, and sizes calculated based on this broadening are in good agreement with widths measured by TEM. The relative peak intensities vary from sample to sample due to different degrees of preferential alignment of the nanorods on the substrate following sample preparation by drop-casting (see Supporting Information). Variations in peak widths for different reflections result from the anisotropic shape of the nanoparticles, with a much longer length parallel to the crystallographic *c*-axis; most obviously, this results in a much narrower diffraction peak for the (002) planes relative to other features (Figure 5C).[26] Overall, these observations corroborate our characterization of the nanorods' composition and structure and verify that the long axis of the rods lies along the crystallographic *c*-axis.

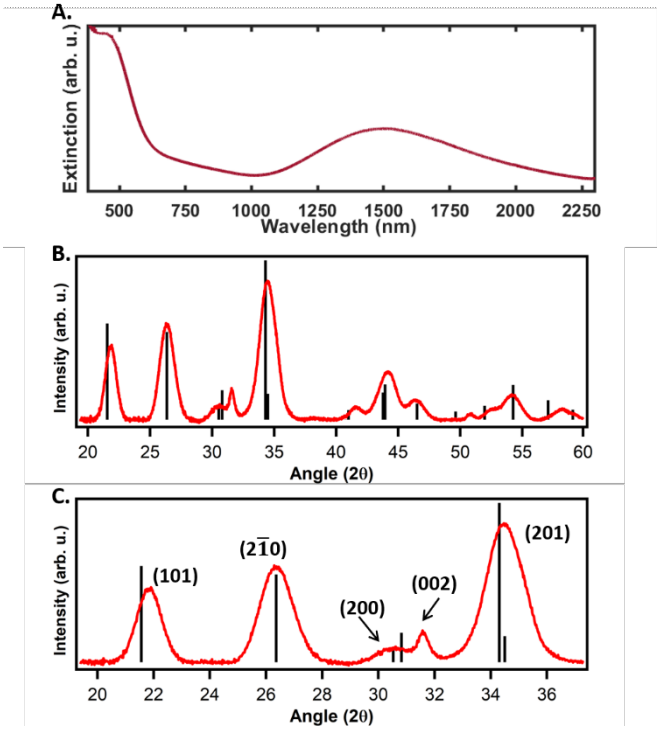

Figure 5. Representative UV-Vis-NIR and powder X-ray diffraction characterization of $BaTiS_3$ nanorods from hot-injection synthesis under standard conditions. A UV-Vis-NIR absorbance spectrum for a nanorod sample, measured in tetrachloroethylene solution, is shown in panel A. Panel (B) compares the measured PXRD data to the reference lines reported for $BaTiS_3$ in the needle-like hexagonal ($P6_3/mmc$) phase. Panel (C) shows a magnified view of the 20° – 37° region of a PXRD measurement of $BaTiS_3$ nanorods, along with the corresponding indexing of each major feature.

Heat-up synthesis: isotropic $BaTiS_3$ nanoparticles. In contrast to the hot-injection synthesis, $BaTiS_3$ nanoparticles synthesized using a heat-up method show little to no shape anisotropy (Figure 6), giving rise to round particles exhibiting uniform Scherrer broadening by PXRD. In this method, in brief, N,N'-diethyldithiourea, $Ba[N(SiMe_3)_2]_2(THF)_2$, and $Ti(NMe_2)_4$ are combined in dry oleylamine in a Schlenk pressure tube and placed in a pre-heated heating mantle in order to rapidly raise the temperature of the reaction solution to 360 °C, resulting in the formation of an inky black solution; after the

desired time, the reaction is cooled and the nanocrystals are isolated and washed with chloroform and ethanol using the same work-up procedure used for the nanorods synthesized by hot-injection. The nanoparticles exhibit similar solubility properties to the nanorods, readily forming colloidal solutions in solvents such as chloroform, although the addition of small quantities of oleylamine after washing is sometimes necessary to maintain colloidal stability. Representative data from a heat-up synthesis is shown in Figure 6.

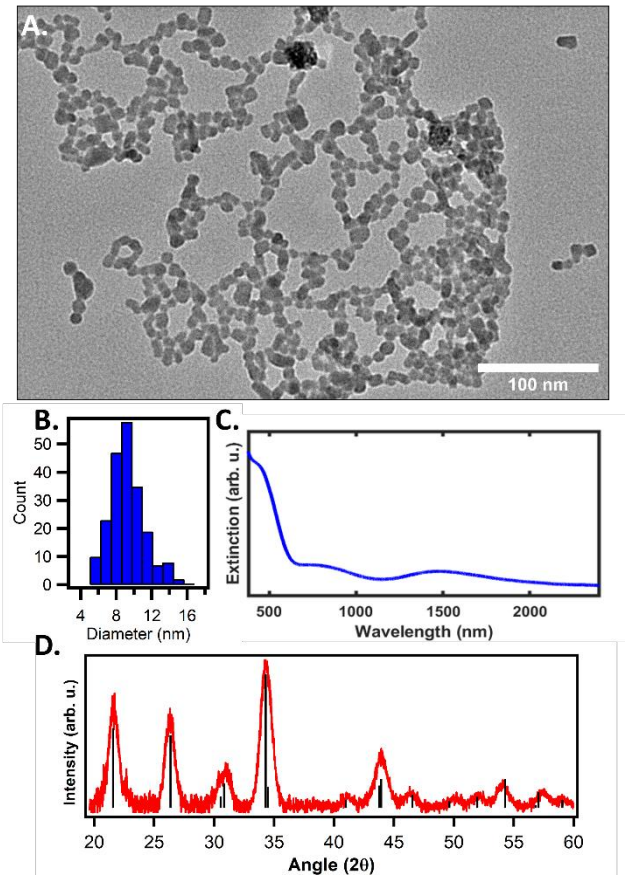

Figure 6. Characterization of a sample of $BaTiS_3$ nanoparticles synthesized using a heat-up protocol at 360 °C with a 1:1:15 Ba:Ti:S ratio and a 2 hour reaction time. (A) shows a TEM image; the scale bar represents 100 nm (Additional TEM images are provided in the Supporting Information). The size distribution of particle diameters is given in panel B; the average size is 9.2 ± 2.0 nm. The UV-Vis-NIR absorbance spectrum (C) taken in tetrachloroethylene shows similar features to those observed for nanorod samples, but in different intensity ratios. Panel D shows the powder XRD diffraction pattern for the sample, overlaid with predicted reference pattern of $BaTiS_3$ in $P6_3/mmc$.

Stoichiometry, off-stoichiometry, and structural variations. Stoichiometric $BaTiS_3$ possesses the $BaNiO_3$ hexagonal structure type, as noted above. However, it is also known that off-stoichiometric compositions (e.g. Ba_xTiS_3, x = 1.00-1.05 and $BaTiS_y$, y = 2.7-3.0) reveal a composite crystal structure characterized by two interpenetrating subcells (one based on the Ba lattice and one on the TiS_3 lattice) with mutually variable *c*-parameters.[27-29] The structures of these off-stoichiometric composite crystals have been described by Saeki *et al.* using a four-dimensional formalism, with c_{TiS3} reflecting the periodicity of the TiS_3 subcell and c_{Ba} representing the periodicity of the Ba chain subcell.[28] The net result in the powder diffraction pattern is the presence of "extra" peaks (not expected for the fully commensurate $c_{TiS3} = c_{Ba}$ structure) as well as small shifts in the positions of the main diffraction peaks resulting from apparent shifts in the lattice parameters (particularly *c*). Similar structural analysis also applies to the related strontium compounds, e.g. $Sr_{1+x}TiS_3$.[30-32]

The deviations we observe in our PXRD data relative to the reference data for stoichiometric $BaTiS_3$ (Figure 5) can be explained in the context of this off-stoichiometry. Because size broadening in our nanocrystal PXRD data precludes the identification of the less intense peaks indexed by Saeki *et al.*, we will refer to the *apparent c* lattice parameter for our structure, which is most obviously correlated with the position of the (002) diffraction peak.[28]

Notably, for sulfur-deficient stoichiometries $BaTiS_y$, significant shifts in the apparent *c* lattice constant are reported for more sulfur-deficient compositions; as *y* decreases, the apparent value of *c* also decreases linearly.[28] For instance, the (002) diffraction peak, appearing at approximately 31-32° in our data, was reported to shift from approximately 31.0° in $BaTiS_{2.93}$ to approximately 33.1° in $BaTiS_{2.70}$. While shifts in *a* were also reported, this effect is much smaller.

In the powder X-ray diffraction data of our nanorods and nanoparticles, we observe significant sample-to-sample variation in the value of the apparent *c* lattice parameter when compared to the reported structural parameters of $BaTiS_3$. This can be observed by comparing the PXRD data shown above for nanorods synthesized by hot injection (Fig 5) and for nanoparticles synthesized by heat-up (Figure 6E); in general, the more isotropic nanoparticles from the heat-up synthesis agree more closely with the reference pattern of the reported $BaTiS_3$ structure, although small shifts in some diffraction peaks can be discerned. The deviations of the nanorod PXRD data from the expected reference pattern are much more significant. Figure 7 overlays the PXRD data from a typical nanorod sample from a hot-injection synthesis to the simulated XRD pattern of $BaTiS_3$ in the $BaNiO_3$ ($P6_3mmc$, *a* = 6.76 Å, *c* = 5.80 Å) structure type;[17] also overlaid is a simulated pattern for $BaTiS_3$ in the same structure type, but with the *c* axis compressed to 5.66 Å and the *a* axis slightly expanded to 6.78 Å.

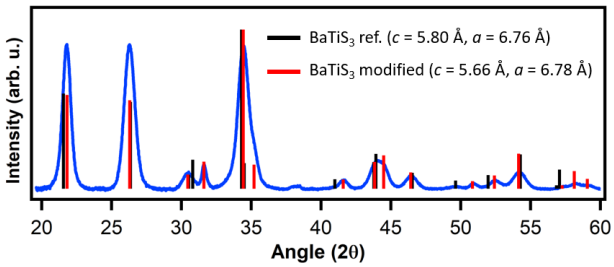

Figure 7. Variation in the powder XRD pattern and structural parameters of $BaTiS_3$ nanorods synthesized by hot injection (nanorods). Nanorod data is shown in blue and compared to calculated reference patterns based on the reported structure for stoichiometric $BaTiS_3$ (black) and a modified lattice for a sulfur-deficient material (red).

The modified structure matches the nanorod data much more closely. The shift is most readily apparent in the (002) diffraction peak, but can also readily be observed in the (101) and (201) peaks (see Figure 5C for labeled peak indexes). The slightly more prominent shoulder on the high-angle side of

the (201) peak in the nanorod sample could be due to the presence of the shifted (102) diffraction peak, but it is not well-resolved due to size-broadening. Generally, little to no shift is observed in the $(2\bar{1}0)$ peak at 26.4°, suggesting that there is at most a small variation in *a*; when small shifts can be discerned, they are generally towards lower angles. This is again consistent with the results of Saeki *et al.* who found that *a* increases slightly with decreasing sulfur content.[28]

Although there is some sample-to-sample variation, across a large number of samples, we observed a consistent pattern that the nanoparticles synthesized by heat-up showed a much closer match to the reported $BaTiS_3$ structure (e.g., Figure 6E; see SI for additional representative data), while the nanorods from the hot-injection synthesis showed a pattern suggestive of a significantly shortened apparent *c*-axis, generally close to 5.6-5.7 Å as shown here. Based on prior studies of the structure of $BaTiS_y$, we attribute this to a more sulfur-deficient stoichiometry in the nanorods synthesized by hot-injection.[28] Notably, this sulfur deficiency occurs despite the use of a ten-fold excess (30 equivalents) of the sulfur source during the reaction. The implications of this for the properties of these nanocrystals will be discussed further below.

Overall, comparison with the data reported previously for bulk composite crystals of the formula $BaTiS_y$ allows the degree of sulfur deficiency to be estimated based on a linear correlation between *y* and the lattice parameters *a* and *c* for the barium sublattice;[28] for example, for the nanorods whose PXRD pattern is shown in Figure 7, *y* is estimated to be approximately 2.87. Note that, for simplicity, we refer to the nanocrystals synthesized in this paper by their nominal $BaTiS_3$ composition, while recognizing that the true stoichiometry may differ.

The barium and titanium content of the nanocrystal samples has been measured by ICP-MS following digestion using aqueous HF/HNO_3. The measured stoichiometry is typically titanium-rich (e.g., a Ti:Ba ratio ranging from 1.05:1 to 1.4:1; see SI for details). More isotropic nanoparticle samples from the heat-up synthesis typically exhibited Ti:Ba ratios closer to stoichiometric (e.g., 1.05:1), while nanorod samples from hot injection tend to be titanium-rich. Two possible explanations are hypothesized for this deviation from ideal stoichiometry, which may operate in concert. First, the barium-deficient stoichiometry is likely to be due at least in part to surface effects; it is well known that the overall stoichiometry of small nanocrystals (with a high surface-to-volume ratio) frequently deviates from the theoretical bulk stoichiometry due to surface termination.[33-35] Given the weak interaction between barium and the TiS_3 chains, the nanorod surfaces are likely Ti/S terminated, with Ba^{2+} cations stripped from the surface during growth or washing. Secondly, it is possible that the sulfur deficiency in the nanorod samples (see above) is charge-compensated by Ba^{2+} vacancies, contributing to the measured barium deficiency. Energy-dispersive X-ray (EDX) measurements of samples imaged by TEM have also been carried out and confirm the presence of barium/titanium and sulfur in the nanorods and nanoparticles; however, accurate quantification using this method is hindered by significant overlap of the most prominent Ti and Ba emission lines (Kα and Lα, respectively).

Synthetic variation and size/shape control. Various modifications to the synthetic methods have been tested in order to delineate our ability to tune the nanocrystal size, shape, and aspect ratio; these studies have focused on the hot-injection methodology because of the increased control over growth conditions afforded by this method. Studies of syntheses with different reaction times suggest that nanorod growth is complete within the first 5 minutes after injection at 360 °C; reaction times between 5 minutes and 30 minutes did not result in further growth or any significant changes to shape and aspect ratio (*vide infra*). Much longer reaction times (e.g. 14 hours) gave particles with poorly controlled size/shape distributions, possibly due to Ostwald ripening processes.

Temperatures as low as 280 °C still gave rise to crystalline $BaTiS_3$ (hot injection method, two hour reaction time—see SI); at 250 °C, the reaction mixture did not undergo the typical color change to black upon injection of the sulfur source, and no black solid material was isolated upon workup, suggesting that no nanocrystal formation occurs at this temperature.

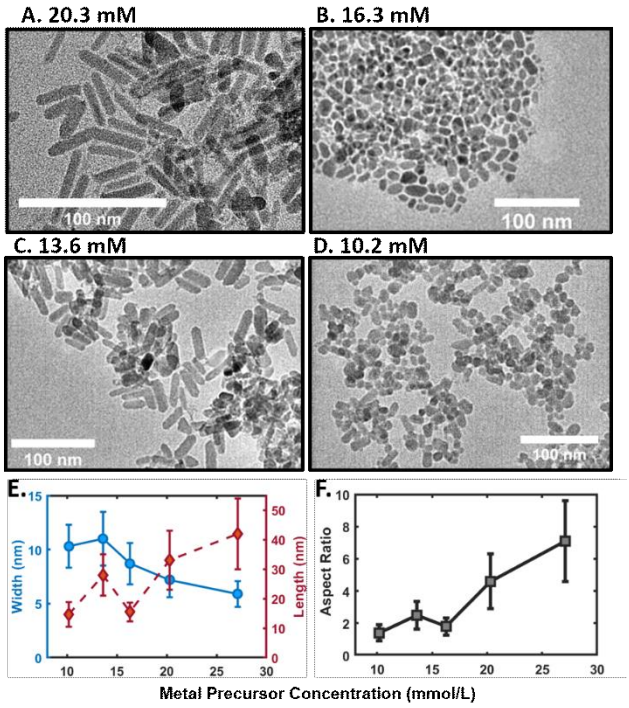

Figure 8. Dependence of nanocrystal length, width, and aspect ratio on the precursor concentration in the reaction mixture. (A-D) TEM images (scale bar 100 nm) of nanorods synthesized at different concentrations, as labeled on the images. (E) Nanorod length (orange) and width (blue) as a function of reaction concentration; on average, length increases and width decreases as concentration increases; error bars represent the standard deviations of the size distributions measured by TEM. (F) Nanorod aspect ratio as a function of reaction concentration.

The nanocrystal width and aspect ratio also showed a distinct dependence on reaction concentration; as the total amount of oleylamine solvent/surfactant is increased from 3 g (standard conditions, 27 mM metal concentrations) to 8 g (dilute conditions, 10 mM metal concentrations), the nanorods increase in width and decrease in length, eventually giving rise to nearly isotropic particles (approximately 1.4:1 aspect ratio). Figure 8 shows TEM images and size/shape data for nanocrystals synthesized at different concentrations of metal precursors (hot injection, 360 °C, 30 minute reaction time).

Therefore, control over reaction temperature and concentration—in addition to the choice of hot injection or heat-up synthesis methods—provide for considerable synthetic control over the nanocrystal shape. Additional data for nanocrystals

synthesized under different conditions is provided in the *Supporting Information*.

Stability. It has been argued that (AE)$M^{IV}S_3$ chalcogenide perovskites and related materials (such as $BaTiS_3$) would have a significant advantage in terms of stability relative to the lead halide perovskites, as noted above. While the stability of these bulk materials has been previously tested,[13] it is not *a priori* obvious that the high stability of bulk materials would translate to nanocrystals, given their high surface area which may make them more prone to surface-initiated degradation reactions involving atmospheric water or oxygen. In order to test the stability of the $BaTiS_3$ nanorods, a sample of material exposed to ambient conditions (room temperature, ~40% humidity) was monitored by powder XRD over the course of 8 weeks (Figure 9A). During this time, although dramatic changes to the diffraction patterns are not observed, the peak width (FWHM) does increase slightly (see Supporting Information). This suggests some loss of crystallinity, possibly due to surface degradation; we hypothesize that a surface oxide layer may form upon exposure to air, as has been previously observed for TiS_2 nanodiscs.[36] However, the nanocrystal samples are not stable to direct immersion in water; after brief immersion (10 seconds), new peaks corresponding to an unidentified decomposition product appear in the PXRD pattern of the sample, and after 20 minutes no diffraction is observed (Figure 9B), suggesting complete destruction of the sample crystallinity. Visually, the originally deep brown-red color of the sample is significantly lightened. These results suggest that while these $BaTiS_3$ nanocrystals maintain some stability under ambient conditions, they may not be as robust overall as bulk materials.

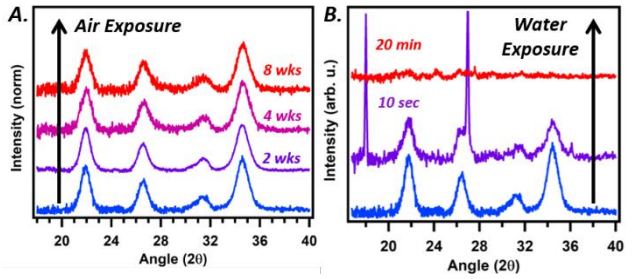

Figure 9. Stability of the $BaTiS_3$ nanoparticles monitored by PXRD. (A) PXRD data on nanocrystals exposed to air under ambient conditions for up to 8 weeks. (B) PXRD data on nanocrystals immersed in water for 10 seconds (purple) or 20 minutes (red).

Optical characterization and shape-dependence of the optical properties. Samples of the $BaTiS_3$ nanorods typically appear red-brown or brown-black in color as solids and give rise to orange-brown colloidal solutions. In the UV-Vis-NIR spectra, both nanorod and isotropic nanoparticle samples show three clearly identifiable absorbance bands (e.g. Figure 5A, 6D) at approximately 2.6 eV (450 nm), 1.5 eV (830 nm), and 0.8 eV (1500 nm). Although these same basic features are discernible in all samples studied, they exhibit sample-dependent variations in their exact positions, broadening, and relative intensities (Figure 10).

There are readily apparent differences in the relative intensities of the three absorbance features in different samples, and especially upon comparing nanorod samples to isotropic (heat-up) samples (Figure 10A). This difference is observable by eye, as heat-up nanoparticle samples typically have a brown-black color while nanorod samples typically have a distinctly reddish-brown color. This difference presumably originates from the greater relative intensity of the broad absorbance feature near 1.5 eV in the isotropic samples (Figure 10A). This feature is only faintly discernible in the spectra of the nanorods. Conversely, the relative intensity of the NIR peak at 0.8 eV is higher for the nanorod samples than for the isotropic nanoparticle samples.

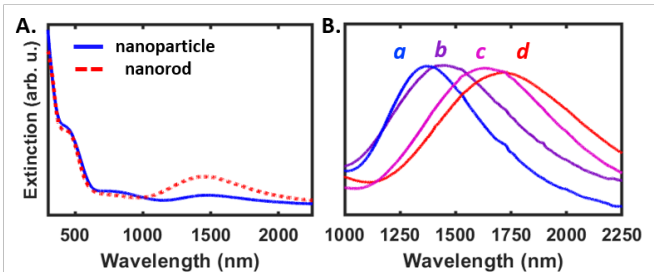

Figure 10. (A) Comparison of the absorbance spectrum of a typical nanorod sample synthesized by hot injection (red, dashed) with the spectrum of a typical nanoparticle sample synthesized by heat-up (blue). (B) Representative nanorod spectra showing wide variation in wavelength position of NIR absorbance peak, ranging from a λ_{max} of 1370 nm (0.90 eV) to 1720 nm (0.72 eV). Average nanorod sizes are (length X width): ***a*** (12 X 7 nm), ***b*** (44 X 6 nm), ***c*** (62 X 6 nm), and ***d*** (50 X 7 nm), showing no consistent correlation of peak position with size or shape.

Interestingly, significant sample-to-sample variation is observed in the prominent near-IR absorbance peak at approximately 1500 nm, especially for nanorod samples. Figure 10B shows this peak for four nanorod samples that illustrate the wide range of energies observed in different samples. Analysis of the position of this peak across a range of samples shows no consistent correlation with nanorod length, width, or aspect ratio; the shift in position does not appear to be related to a size effect such as quantum confinement. For the isotropic particles, the position of this peak varies less widely, occurring between about 1520-1570 nm for particles synthesized under the standard heat-up conditions. The absorbance spectrum was also measured in several solvents (chloroform, tetrachloroethylene, dichloroethane—see SI) and no change in peak position could be measured, although it is possible that a shift would be observed in solvents with more widely varying dielectric constants.

Time-dependent structural and spectroscopic properties during nanorod growth. As noted above, during the standard hot-injection synthesis at 360 °C, the nanorod growth appears to be essentially complete within 5 minutes. To further confirm and probe the evolution of the nanorod properties during the reaction time, we removed aliquots from a standard hot-injection reaction solution at 5, 10, 15, and 30 minutes following injection of the sulfur precursor at 360 °C; results from the characterization of these aliquots are shown in Figure 11. As expected, there is no significant change in the average length and width of the nanocrystals during this time, as determined by TEM (Figure 11B). However, there are significant changes in the UV-Vis-NIR absorbance spectra and in the powder XRD patterns of the nanorods. In particular, the NIR absorbance peak shifts steadily to higher energy and increases in relative intensity over the course of the reaction time (Figure 11C-D). Simultaneously, shifts in the PXRD pattern consistent with a contraction of the apparent *c* axis—attributed to increasing sulfur deficiency in the lattice, see discussion above—are observed (Figure 11D). This data em-

phasizes that although both of these characteristics (off-stoichiometry/structure and NIR absorbance) are correlated, they are not (solely) dependent on particle size/shape or on reaction stoichiometry, temperature, or concentration.

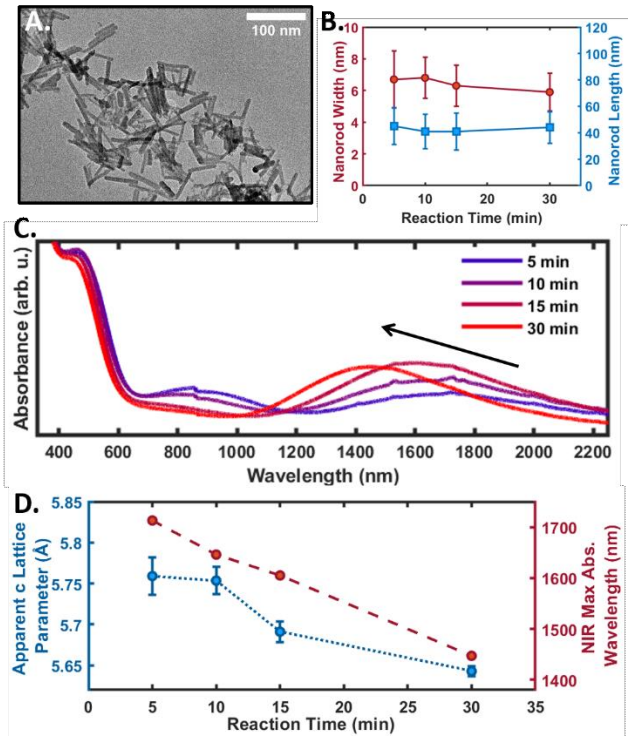

Figure 11. (A) Representative TEM image of the particles used in this time-series experiment, taken after 10 minutes of reaction. (B) Nanorod width (red circles, left axis) and length (blue squares, right axis) as a function of reaction time follow hot injection. (C) Spectral evolution as a function of reaction time (reaction progresses from blue to red, following arrow direction); absorbance intensity is arbitrarily scaled. (D) Scatter plot of the NIR absorbance peak λ_{max} (red) and the apparent *c* lattice parameter measured by PXRD (blue) as a function of reaction time.

Correlation of spectroscopic properties, structural parameters, and off-stoichiometry. While the exact cause of the variations in the structural and optical properties of the $BaTiS_3$ nanorods and nanoparticles is still under investigation, the data presented above suggests that the structural and stoichiometric variations (in particular, the sulfur deficiency which is reflected in changes to the apparent unit cell parameters) are intimately related to the spectroscopic changes observed—in particular, the variable position of the strong NIR absorbance peak in the nanorods. Figure 12 further illustrates this connection by plotting the correlation between the apparent crystallographic *c* axis of the nanorods and the λ_{max} of the NIR absorbance peak for a wide range of samples synthesized with varying reaction conditions (time, temperature, concentration, stoichiometry). There is a distinct, albeit noisy, correlation. There are likely multiple factors that influence both the structure and the absorbance peak position; for instance, the Ba/Ti stoichiometry in the crystal lattice is also known to influence *c*.[27]

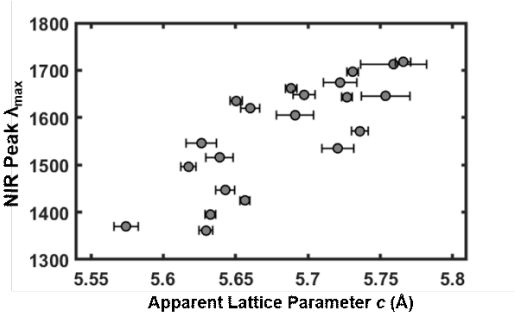

Figure 12. Correlation between the apparent *c* lattice parameter (from PXRD analysis) and the NIR peak absorbance maximum in a range of $BaTiS_3$ nanorod samples. Error bars represent the estimated standard deviations in the lattice parameters determined by Rietveld refinement of the PXRD data.

These results are reminiscent of the properties of nanomaterials such as copper sulfide, $Cu_{2-x}S$, and related materials, where off-stoichiometric compositions give rise to strong absorbance peaks in the visible to NIR regions which arise from localized surface plasmon resonances (LSPRs) due to the presence of free charge carriers (holes, in the case of $Cu_{2-x}S$).[37-41] It is possible that a similar phenomenon in $BaTiS_y$ is responsible for our observations, which would make $BaTiS_y$ a relatively rare example of a non-copper-containing chalcogenide nanocrystal exhibiting LSPR resonances;[42] we do note that the observation of an LSPR absorbance in TiS_2 nanosheets has been proposed.[43] The fact that the energy of the observed NIR absorbance peak increases with increasing off-stoichiometry would be consistent with this hypothesis. However, further work is needed to establish whether or not this optical feature truly arises from free carriers.

CONCLUSIONS

In summary, we have demonstrated a wet-chemical method for the synthesis of $BaTiS_3$ nanorods and nanoparticles that allows for the nanocrystal size and aspect ratio to be controlled through choice of synthesis method and reaction conditions. Under standard conditions, $BaTiS_3$ nanorods are produced upon injection of a sulfur source into a precursor solution of Ba^{2+} and Ti^{2+} amides at 360 °C, although we found that crystalline nanorods were formed at temperatures as low as 280 °C. We found that the structural features of the nanoparticles and nanorods are closely analogous to those found in the bulk material, including the presence of a composite crystal structure with incommensurate Ba and TiS_3 lattices, with the structural parameters tied to the stoichiometry of the material. Deviations from the ideal lattice parameters are attributed to sulfur deficiency and are correlated to variations in energy of a strong near-IR absorbance peak observed in nanorod samples. The nature of this spectroscopic feature is still under investigation. However, we cannot rule out that the structural properties of the nanocrystals may deviate in unrecognized ways from the bulk crystals, and further detailed investigation of the structural and surface properties of these nanomaterials is warranted. In particular, the presence of a surface oxide layer or the incorporation of small amounts of oxygen impurities into the material could have an important impact on the optical/electronic properties and potential applications of these materials.

This work demonstrates the feasibility of the synthesis of $(AE)M^{IV}E_3$ materials in solution at readily accessible temperatures. It is likely that this methodology can be extended to

other (AE)TiS_3 materials such as $SrTiS_3$ and $CaTiS_3$, and it is possible that similar routes could be used to access a more diverse range of (AE)$M^{IV}E_3$ materials. Some of these materials (including $BaZrS_3$, $CaZrS_3$, $SrZrS_3$, $CaZrSe_3$, $BaHfS_3$, and $CaHfS_3$) are known to adopt a distorted perovskite structure under at least some conditions, characterized by a three-dimensional network of corner-sharing MS_6 octahedra;[44-46] by analogy to lead-halide perovskites, these chalcogenide perovskites have been proposed as potential photovoltaic absorbers.[1-3, 12, 14, 47-49] In some cases, the theoretical maximum efficiency rivals or exceeds that of the lead halide perovskites, and they are expected to be more stable, in addition to being less toxic and more environmentally friendly.[2, 3] However, experimental progress in realizing efficient photovoltaic devices using these chalcogenide perovskites has been slow, in part due to synthetic challenges; solution routes to colloidal nanocrystals, as described here, could present one possible approach towards overcoming these challenges.

EXPERIMENTAL SECTION

General. All synthetic manipulations were carried out under an atmosphere of ultrapure argon or dinitrogen gas in a glove box or using a Schlenk line unless otherwise stated. $Ba[N(SiMe_3)_2]_2(THF)_2$ was synthesized according to previous reports, recrystallized from pentane, and stored in an N_2 glovebox.[50] Tetrakis(dimethylamido)titanium was purchased from Acros Organics, stored in an N_2 glovebox, and used as received. N,N'-Diethylthiourea was purchased from Alfa Aesar and purified by recrystallization from benzene, followed by drying at 60 °C in vacuo overnight, prior to use. Oleylamine (70%) was purchased from Sigma-Aldrich and refluxed in vacuo at 120 °C over CaH_2 for two hours before distilling in vacuo, then stored over 4 Å molecular sieves in an N_2 glovebox prior to use. All other solvents used for nanocrystal workup were standard reagent grades and were used as received. ***Caution!*** *Benzene is a known carcinogen and should be handled in an efficient fume hood by trained personnel wearing appropriate PPE.*

X-ray diffraction. Samples for powder X-ray diffraction were dropcast from solution onto pieces of silicon <100> or onto a zero-background silicon plate. In some cases, nanocrystal samples were washed an additional time by precipitating from solution with butanol or ethanol prior to XRD analysis in order to remove excess ligands. PXRD data was collected using Cu Kα radiation with an AXRD Benchtop diffractometer from Proto Manufacturing equipped with a Dectris MYTHEN2 R 1D hybrid photon-counting detector in Bragg-Brentano geometry. The step size was 0.020° and dwell times between 5-15 seconds were used. Except where stated otherwise, the reference pattern for $BaTiS_3$ is taken from ICSD Coll. Code #14175.[4] Further information about PXRD data analysis is provided in the Supporting Information.

UV-Vis-NIR. Samples for solution absorbance measurements were dispersed in an appropriate solvent (chloroform or tetrachloroethylene) by sonicating briefly, transferred to a quartz cuvette, and then measured using a Perkin Elmer Lambda 900 spectrometer.

Transmission electron microscopy (TEM): Samples for TEM were dispersed at low concentration in chloroform by sonicating for several minutes, then a drop of the resulting colloidal dispersion was allowed to air-dry on a carbon-coated copper TEM grid. Samples were dried in a vacuum dessicator overnight prior to analysis. Imaging was performed using a JEOL 2100 TEM operating at 200 kV, and an Oxford EDS system was used for EDS analysis. TEM size distributions (length and width) were calculated based on measurements of at least 100 individual nanoparticles, and error bars on size measurements represent the standard deviations of these distributions.

ICP-MS. For ICP-MS analysis, an aliquot of known volume of a stock nanocrystal solution was dried under a stream of air to remove volatile solvent, and then digested by heating for two hours in a 3:1 mixture of ultrapure hydrofluoric acid and nitric acid. The sample was diluted with ultrapure water, filtered, and then subjected to analysis by ICP-MS using a Perkin Elmer ELAN DRC II instrument. The results were compared to a calibration curve constructed using Ba and Ti standards purchased from Ricca Chemical. ***Caution!*** *Hydrofluoric acid is extremely toxic and corrosive; it should only be handled by individuals specifically trained in its use, using appropriate personal protective equipment, and in an efficient fume hood. Appropriate first aid should be readily available when HF is in use and if any exposure to vapor or liquid occurs, treatment should be started immediately*.[51]

Synthesis of $BaTiS_3$ nanorods by hot injection: In a typical reaction, $Ba[N(SiMe_3)_2]_2(THF)_2$ (60.2 mg, 0.1 mmol) is dissolved in dried and degassed oleylamine (2.5 g) in a 25 mL three-necked round-bottom flask under N_2 in a glovebox. To this mixture is injected $Ti(NMe_2)_4$ (22.4 mg (23.5 μL), 0.1 mmol). The flask is equipped with a reflux condenser and sealed prior to being brought out of the glovebox and transferred to a Schlenk line where it is placed back under N_2 or argon. The reaction mixture is then heated to 360° C using a temperature-controlled heating mantle. Separately, a solution of N,N'-diethylthiourea (0.5 g, 3 mmol) is prepared in dried and degassed oleylamine (0.5 g) and fully dissolved by heating to 80 °C under nitrogen for 5 minutes with vigorous stirring. When the reaction mixture reaches 360 °C, the diethylthiourea solution is rapidly injected into the reaction mixture, resulting in an immediate color change to black. The reaction mixture is then allowed to stir at this temperature for between 5 minutes to 14 hours. ***Caution!*** *Heating reaction mixtures at high temperatures presents a potential fire risk and should be carried out with caution by trained personnel, and appropriate fire safety equipment should be readily available.* At the end of this time, the heating mantle is removed and the reaction mixture is allowed to passively cool to room temperature. The remainder of the workup, purification, and analysis is carried out under air without any special precautions. The reaction mixture is diluted with chloroform, and then ethanol is added to precipitate the nanocrystals. The nanocrystals are isolated by centrifugation at 3500 rpm. The precipitated nanocrystals are washed two additional times with ethanol and then once with chloroform; in each case the precipitated nanocrystals are isolated by centrifugation at 3500 rpm. The precipitate is resuspended in chloroform with sonication and then centrifuged at low speed (1000 rpm) for 5 minutes; a small amount of precipitated solids are discarded and the majority of the nanocrystals remain in the supernatant and are used for further analysis. If needed to improve the colloidal stability of the nanomaterials, 60 μL of oleylamine are added to the chloroform solution, followed by brief sonication to produce a colloidal suspension of nanocrystals.

Synthesis of $BaTiS_3$ nanoparticles by heat-up. In a typical reaction, $Ba[N(SiMe_3)_2]_2(THF)_2$ (60.2 mg, 0.1 mmol), $Ti(NMe_2)_4$, (22.4 mg, 0.1 mmol) and N,N'-diethylthiourea (0.396 g, 3 mmol) are combined in oleylamine (3 g) in a Schlenk pressure tube under N_2, and the reaction mixture was heated to 360 °C and maintained at this temperature for 2 hours. The flask was

allowed to cool to room temperature and the nanocrystals were worked up, purified, and resuspended as described above for the hot injection synthesis. ***Caution!*** *Heating a sealed reaction vessel presents a potential explosion risk. Appropriate high-quality, thick-walled glassware should be used and the reaction should be carried out behind a safety shield.*

ASSOCIATED CONTENT

Supporting Information. Further characterization data (TEM, UV-Vis, PXRD) for nanocrystals synthesized under various conditions. This material is available free of charge via the Internet at http://pubs.acs.org.

AUTHOR INFORMATION

Corresponding Author

* screutz@chemistry.msstate.edu

Author Contributions

The manuscript was written through contributions of all authors.

ACKNOWLEDGMENT

This research was supported by the National Science Foundation under Award (DMR-2004421). Mr. Bruno Donnadieu is acknowledged for assistance with powder X-ray crystallography. Mr. Chanaka Navarantha is acknowledged for assistance with ICP-MS measurements. Dr. RoobanVenkatesh Kulandaivelu Govindarajulu Thirumalai and Dr. I-Wei Chu are thanked for assistance with TEM measurements.

REFERENCES

1. Swarnkar, A.; Mir, W. J.; Chakraborty, R.; Jagadeeswararao, M.; Sheikh, T.; Nag, A., Are chalcogenide perovskites an emerging class of semiconductors for optoelectronic properties and solar cell? *Chem. Mater.* **2019,** *31*, 565-575.

2. Sun, Y.-Y.; Agiorgousis, M. L.; Zhang, P.; Zhang, S., Chalcogenide perovskites for photovoltaics. *Nano Lett.* **2015,** *15*, 581-585.

3. Meng, W.; Saparov, B.; Hong, F.; Wang, J.; Mitzi, D. B.; Yan, Y., Alloying and defect control within chalcogenide perovskites for optimized photovoltaic application. *Chem. Mater.* **2016,** *28*, 821-829.

4. Huster, J., Die kristallstruktur von $BaTiS_3$. *Z. Naturforsch. B* **1980,** *35*, 775-775.

5. Clearfield, A., The synthesis and crystal structures of some alkaline earth titanium and zirconium sulfides. *Acta Cryst.* **1963,** *16*, 135-142.

6. Brehm, J. A.; Bennett, J. W.; Schoenberg, M. R.; Grinberg, I.; Rappe, A. M., The structural diversity of ABS_3 compounds with d^0 electronic configuration for the B-cation. *J. Chem. Phys.* **2014,** *140*, Art. No. 224703.

7. Niu, S.; Joe, G.; Zhao, H.; Zhou, Y.; Orvis, T.; Huyan, H.; Salman, J.; Mahalingam, K.; Urwin, B.; Wu, J.; Liu, Y.; Tiwald, T. E.; Cronin, S. B.; Howe, B. M.; Mecklenburg, M.; Haiges, R.; Singh, D. J.; Wang, H.; Kats, M. A.; Ravichandran, J., Giant optical anisotropy in a quasi-one-dimensional crystal. *Nat. Photonics* **2018,** *12*, 392-396.

8. Wu, J.; Wang, N.; Yan, X.; Wang, H., Emerging low-dimensional materials for mid-infrared detection. *Nano Res.* **2021,** *14*, 1863-1877.

9. Wu, J.; Cong, X.; Niu, S.; Liu, F.; Zhao, H.; Du, Z.; Ravichandran, J.; Tan, P. H.; Wang, H., Linear dichroism conversion in quasi-1D perovskite chalcogenide. *Adv. Mater.* **2019,** *31*, 1902118.

10. Paudel, T. R.; Tsymbal, E. Y., Evaluating the thermoelectric properties of $BaTiS_3$ by density functional theory. *ACS Omega* **2020,** *5*, 12385-12390.

11. Sun, B.; Niu, S.; Hermann, R. P.; Moon, J.; Shulumba, N.; Page, K.; Zhao, B.; Thind, A. S.; Mahalingam, K.; Milam-Guerrero, J.; Haiges, R.; Mecklenburg, M.; Melot, B. C.; Jho, Y.-D.; Howe, B. M.; Mishra, R.; Alatas, A.; Winn, B.; Manley, M. E.; Ravichandran, J.; Minnich, A. J., High frequency atomic tunneling yields ultralow and glass-like thermal conductivity in chalcogenide single crystals. *Nature Commun.* **2020,** *11*, Art. No. 6039.

12. Niu, S.; Huyan, H.; Liu, Y.; Yeung, M.; Ye, K.; Blankemeier, L.; Orvis, T.; Sarkar, D.; Singh, D. J.; Kapadia, R.; Ravichandran, J., Bandgap control via structural and chemical tuning of transition metal perovskite chalcogenides. *Adv. Mater.* **2017,** *29*, 1604733.

13. Niu, S.; Milam-Guerrero, J.; Zhou, Y.; Ye, K.; Zhao, B.; Melot, B. C.; Ravichandran, J., Thermal stability study of transition metal perovskite sulfides. *J. Mater. Res.* **2018,** *33*, 4135-4143.

14. Perera, S.; Hui, H.; Zhao, C.; Xue, H.; Sun, F.; Deng, C.; Gross, N.; Milleville, C.; Xu, X.; Watson, D. F.; Weinstein, B.; Sun, Y.-Y.; Zhang, S.; Zeng, H., Chalcogenide perovskites -- an emerging class of ionic semiconductors. *Nano Energy* **2016,** *22*, 129-135.

15. Wang, Y.; Sato, N.; Yamada, K.; Fujino, T., Synthesis of $BaZrS_3$ in the presence of excess sulfur. *J. Alloys Compd.* **2000,** *311*, 214-223.

16. Cuya, J.; Sato, N.; Yamamoto, K.; Takahashi, H.; Muramatsu, A., thermogravimetric study for the reaction of $BaTiO_3$ with CS_2 by using quartz spring-type thermobalance. *High Temp. Mater. Processes* **2003,** *22*, 197-201.

17. Clearfield, A., The synthesis and crystal structures of some alkaline earth titanium and zirconium sulfides. *Acta Cryst.* **1963,** *16*, 135-142.

18. Buffiere, M.; Dhawale, D. S.; El-Mellouhi, F., Chalcogenide materials and derivatives for photovoltaic applications. *Energy Technol.* **2019**, 1900819.

19. Wei, X.; Hui, H.; Zhao, C.; Deng, C.; Han, M.; Yu, Z.; Sheng, A.; Roy, P.; Chen, A.; Lin, J.; Watson, D. F.; Sun, Y.-Y.; Thomay, T.; Yang, S.; Jia, Q.; Zhang, S.; Zeng, H., Realization of $BaZrS_3$ chalcogenide perovskite thin films for optoelectronics. *Nano Energy* **2020,** *68*, 104317.

20. Comparotto, C.; Davydova, A.; Ericson, T.; Riekehr, L.; Moro, M. V.; Kubart, T.; Scragg, J., Chalcogenide perovskite $BaZrS_3$: Thin film growth by sputtering and rapid thermal processing. *ACS Appl. Energy Mater.* **2020,** *3* (3), 2762-2770.

21. Ravi, V. K.; Yu, S. H.; Rajput, P. K.; Nayak, C.; Bhattacharyya, D.; Chung, D. S.; Nag, A., Colloidal $BaZrS_3$ chalcogenide perovskite nanocrystals for thin film device fabrication. *Nanoscale* **2021,** *13*, 1616-1623.

22. Hendricks, M. P.; Campos, M. P.; Cleveland, G. T.; Plante, I. J.-L.; Owen, J. S., A tunable library of substituted thiourea precursors to metal sulfide nanocrystals. *Science* **2015,** *348*, 1226-1230.

23. Marcotrigiano, G.; Peyronel, G.; Battistuzzi, R., Kinetics of the desulphuration of ^{35}S-labelled thiourea in sodium hydroxide studied by chromatographic methods. *J. Chem. Soc., Perkin Trans. 2* **1972**, 1539-1541.

24. García-Rodríguez, R.; Hendricks, M. P.; Cossairt, B. M.; Liu, H.; Owen, J. S., Conversion reactions of cadmium chalcogenide nanocrystal precursors. *Chem. Mater.* **2013,** *25*, 1233-1249.

25. Huster, J., Die Kristallstruktur von $BaTiS_3$. *Z. Naturforsch. B* **1980,** *35*, 775.

26. Holder, C. F.; Schaak, R. E., Tutorial on powder X-ray diffraction for characterizing nanoscale materials. *ACS Nano* **2019,** *13*, 7359-7365.

27. Saeki, M.; Onoda, M., Preparation of chain-type composite crystal, Ba_xTiS_3 (x = 1.00-1.05). *J. Solid State Chem.* **1994,** *112*, 65-69.

28. Saeki, M.; Onoda, M.; Yajima, Y., Composite crystals $BaTiS_y$ (y = 2.70-2.93). *J. Solid State Chem.* **1996,** *121*, 451-456.

29. van Smaalen, S., Incommensurate crystal structures. *Crystallograph. Rev.* **2006,** *4*, 79-202.
30. Onoda, M.; Saeki, M.; Yamamoto, A.; Kato, K., Structure refinement of the incommensurate composite crystal $Sr_{1.145}TiS_3$ through the Rietveld analysis process. *Acta Cryst. B* **1993,** *49*, 929-936.
31. Saeki, M.; Onoda, M., Preparation of a new strontium titanium sulfide Sr_xTiS_3 (x = 1.05 - 1.22) with infinitely adaptive structures. *J. Solid State Chem.* **1993,** *102*, 100-105.
32. Gourdon, O.; Petricek, V.; Evain, M., A new structure type in the hexagonal perovskite family; structure determination of the modulated misfit compound $Sr_{9/8}$TiS3. *Acta Cryst. B* **2000,** *56*, 409-418.
33. Jasieniak, J.; Mulvaney, P., From Cd-Rich to Se-Rich – the manipulation of CdSe nanocrystal surface stoichiometry. *J. Am. Chem. Soc.* **2007,** *129*, 2841-2848.
34. Dai, Q.; Wang, Y.; Li, X.; Zhang, Y.; Pellegrino, D. J.; Zhao, M.; Zou, B.; Seo, J.; Wang, Y.; Yu, W. W., Size-dependent composition and molar extinction coefficient of PbSe semiconductor nanocrystals. *ACS Nano* **2009,** *3*, 1518-1524.
35. Morrison, C.; Sun, H.; Yao, Y.; Loomis, R. A.; Buhro, W. E., Methods for the ICP-OES analysis of semiconductor materials. *Chem. Mater.* **2020,** *32*, 1760-1768.
36. Han, J. H.; Lee, S.; Yoo, D.; Lee, J.-H.; Jeong, S.; Kum, J.-G.; Cheon, J., Unveiling chemical reactivity and structural transformation of two-dimensional layered nanocrystals. *J. Am. Chem. Soc.* **2013,** *135*, 3736-3739.
37. Luther, J. M.; Jain, P. K.; Ewers, T.; Alivisatos, A. P., Localized surface plasmon resonances arising from free carriers in doped quantum dots. *Nat. Mater.* **2011,** *10*, 361-366.
38. Rachkov, A. G.; Schimpf, A. M., Colloidal synthesis of tunable copper phosphide nanocrystals. *Chem. Mater.* **2021,** *33*, 1394-1406.
39. Lee, S.; Ghosh, S.; Hoyer, C. E.; Liu, H.; Li, X.; Holmberg, V. C., Iron-content-dependent, quasi-static dielectric resonances and oxidative transitions in bornite and chalcopyrite copper iron sulfide nanocrystals. *Chem. Mater.* **2021,** *33*, 1821-1831.
40. Liu, Y.; Liu, M.; Swihart, M. T., Plasmonic copper sulfide-based materials: A brief introduction to their synthesis, doping, alloying, and applications. *J. Phys. Chem. C* **2017,** *121*, 13435-13447.
41. Coughlan, C.; Ibanez, M.; Dobrozhan, O.; Singh, A.; Cabot, A.; Ryan, K. M., Compound copper chalcogenide nanocrystals. *Chem. Rev.* **117,** *117*, 5865-6109.
42. Gong, M.; Ewing, D.; Casper, M.; Stramel, A.; Elliot, A.; Wu, J. Z., Controllable synthesis of monodispersed $Fe_{1-x}S_2$ nanocrystals for high-performance optoelectronic devices. *ACS Appl. Mater. Interfaces* **2019,** *11*, 19286-19293.
43. Zhu, Z.; Zou, Y.; Hu, W.; Li, Y.; Gu, Y.; Cao, B.; Guo, N.; Wang, L.; Song, J.; Zhang, S.; Gu, H.; Zeng, H., Near-infrared plasmonic 2D semimetals for applications in communication and biology. *Adv. Func. Mater.* **2016,** *26*, 1793-1802.
44. Lelieveld, R.; IJdo, D. J. W., Sulphides with the $GdFeO_3$ structure. *Acta Cryst. B* **1980,** *36*, 2223-2226.
45. Lee, C.-S.; Kleinke, K. M.; Kleinke, H., Synthesis, structure, and electronic and physical properties of the two $SrZrS_3$ modifications. *Solid State Sci.* **2005,** *7*, 1049-1054.
46. Brehm, J. A.; Bennett, J. W.; Schoenberg, M. R.; Grinberg, I.; Rappe, A. M., The structural diversity of ABS_3 compounds with d^0 electronic configuration for the B-cation. *J. Chem. Phys.* **2014,** *140*, 224703.
47. Ju, M.-G.; Dai, J.; Ma, L.; Zeng, X. C., Perovskite chalcogenides with optimal bandgap and desired optical absorption for photovoltaic devices. *Adv. Energy Mater.* **2017,** *7*, 1700216.
48. Nishigaki, Y.; Nagai, T.; Nishiwaki, M.; Aizawa, T.; Kozawa, M.; Hanzawa, K.; Kato, Y.; Sai, H.; Hiramatsu, H.; Hosono, H.; Fujiwara, H., Extraordinary strong band-edge absorption in distorted chalcogenide perovskites. *RRL Solar* **2020,** *4*, 1900555.
49. Hanzawa, K.; Iimura, S.; Hiramatsu, H.; Hosono, H., Material design of green-light-emitting semiconductors: perovskite-type sulfide $SrHfS_3$. *J. Am. Chem. Soc.* **2019,** *141*, 5343-5349.
50. Vaartstra, B. A.; Huffman, J. C.; Streib, W. E.; Caulton, K. G., Syntheses and structures of a series of very low coordinate barium compounds: $Ba[N(SiMe_3)_2]_2(THF)_2$, $\{Ba[N(SiMe_3)_2)]_2(THF)\}_2$, and $\{Ba[N(SiMe_3)_2]_2\}_2$. *Inorg. Chem.* **1991,** *30*, 121-125.
51. Segal, E. B., First aid for a unique acid, HF: A sequel. *Chem. Health. Saf.* **2000,** *7*, 18-23.

TOC GRAPHIC